

Investigation of UH-60A Rotor Structural Loads From Flight and Wind Tunnel Tests

Hyeonsoo Yeo

Mark Potsdam

US Army Aviation Development Directorate
Aviation & Missile Research, Development & Engineering Center
Research, Development, and Engineering Command
Ames Research Center, Moffett Field, California

Thomas R. Norman

National Aeronautics and Space Administration
Ames Research Center, Moffett Field, California

ABSTRACT

NASA/Army UH-60A Airloads Program flight test and full-scale UH-60A Airloads wind tunnel test data are investigated in order to better understand and predict the chord bending moments, one of the unresolved issues in the UH-60A rotor loads prediction. Coupled Helios/RCAS analysis is performed and the calculated rotor loads are compared with the test data. RCAS alone analysis is also performed by applying measured airloads from the tests as prescribed external loads. Effects of the lag damper model are examined by calculating lag damper loads using a nonlinear lag damper model or by applying measured lag damper loads as prescribed external loads. Both airloads and damper loads are important for the accurate prediction of chord bending moments. The calculated chord bending moments with the prescribed measured airloads and measured damper loads show the best correlation with the wind tunnel test data. In particular, the 4 and 5/rev harmonic correlation is excellent. The effects of drive train dynamics and hub impedance on the chord bending moments appear to be very small for the wind tunnel test. Those effects may still be important for the flight test vehicle, although they might be smaller than what was suggested in previous studies.

NOTATION

A	rotor disk area
a	speed of sound
C_{CBM}	chord bending moment coefficient, $M_{CB}/\rho(\Omega R)^2AR$
C_{FBM}	flap bending moment coefficient, $M_{FB}/\rho(\Omega R)^2AR$
C_{Mx}	hub rolling moment coefficient, $M_x/\rho(\Omega R)^2AR$
C_{My}	hub pitching moment coefficient, $M_y/\rho(\Omega R)^2AR$
C_{TM}	torsion moment coefficient, $M_T/\rho(\Omega R)^2AR$
C_T	rotor thrust coefficient, $T/\rho(\Omega R)^2A$
c	blade chord
l	section lift per unit length
$M^2_{c_l}$	section lift coefficient, $l/\frac{1}{2}\rho a^2c$
$M^2_{c_m}$	section pitching moment coefficient, $m/\frac{1}{2}\rho a^2c^2$
M_{CB}	blade chord bending moment
M_{FB}	blade flap bending moment
M_T	blade torsion moment
M_{tip}	hover tip Mach number
M_x	hub rolling moment

M_y	hub pitching moment
m	section pitching moment per unit length
R	rotor radius
T	rotor thrust
α_c	corrected shaft angle, positive backward tilt
μ	advance ratio
ρ	freestream density
σ	rotor solidity
Ω	rotor angular velocity

INTRODUCTION

Rotorcraft aeromechanics prediction capability using coupled computational fluid dynamics (CFD) / rotorcraft comprehensive analysis (CA) has advanced significantly in recent years (Refs. 1–7). For the loads analysis of a UH-60A rotor, three challenging level flight conditions (high speed C8534, low speed C8513, and high thrust C9017) of the NASA/Army UH-60A Airloads Program flight test data (Ref. 8) have been extensively studied using various combinations of CFD/CA tools (Refs. 1, 9–13). Figure 1 shows the UH-60A Airloads aircraft in flight. All the coupled analyses, in general, show satisfactory airloads correlation with the test data. However,

Presented at the AHS 72nd Annual Forum, West Palm Beach, FL, May 17–19, 2016. This is a work of the U.S. Government and is not subject to copyright protection in the U.S. DISTRIBUTION STATEMENT A. Approved for public release; distribution is unlimited.

the prediction of the structural loads did not show the same level of correlation. Although flap bending and torsion moment correlation was reasonably good, chord bending moment correlation was particularly poor. In Ref. 13, the coupled CFD/CA analyses significantly underpredicted peak-to-peak chord bending moments, especially 4/rev harmonic amplitude. The effects of drive train dynamics were examined using a simple one degree-of-freedom shaft drive train model, which consists of polar mass moment of inertia, spring stiffness, and damping. Moment of inertia values were varied with a fixed stiffness value to simulate the high frequency drive train modes. The overall correlation in the half peak-to-peak magnitude and 4/rev harmonic component started to improve with a smaller moment of inertia value. This result showed that the dynamic coupling between the rotor and the drive train is likely a key contributor for the improvement of chord bending moment correlation. However, due to the limitations of the simple drive train model used in the parametric variations, this study also suggested that a more complex drive train model, which can capture higher frequency modes, should be developed and incorporated into the analysis.

A more recent full-scale UH-60A Airloads wind tunnel test at the National Full-Scale Aerodynamics Complex (NFAC) 40- by 80-Foot Wind Tunnel (Ref. 14) provides another set of airloads and structural loads measurements. Figure 2 shows the UH-60A rotor blades installed on the NFAC Large Rotor Test Apparatus (LRTA) in the wind tunnel test section. One of the objectives of the wind tunnel test was to provide data to help evaluate the differences between full-scale wind tunnel and full-scale flight tests. To accomplish this, data were acquired at a limited number of conditions matching those tested during the flight tests. Detailed data comparisons between the wind tunnel and flight test data were performed in Ref. 15. Blade section airloads (normal force and pitching moment) generally agree well between the tests, although noticeable differences were observed in pitching moment at 92%R. Blade flap bending and torsion moments also agree well between the tests. However, there were substantial differences in chord bending moments, especially the 4/rev and 5/rev harmonic components. This study recommended that the potential effects of the drive train dynamics and in-plane hub motion be further investigated.

The present paper investigates the UH-60A rotor structural loads from the flight and wind tunnel tests to better understand the differences in chord bending moments observed in Ref. 15 and to better predict these moments. Coupled CFD and CA analysis predictions of rotor structural loads as well as airloads results are compared with the test data. Structural loads are also calculated by applying measured airloads from the tests as prescribed external loads. By prescribing the measured airloads, the coupled aeroelastic response problem is reduced to one involving only structural dynamics. This may help to identify whether sources of inaccuracies in the structural loads prediction originate from deficiencies in aerodynamics or structural dynamics. For both coupled and prescribed measured airloads analyses, the effects of the lag damper model are examined by calculating lag damper loads

using a nonlinear lag damper model or by applying measured lag damper loads as prescribed external loads.

DESCRIPTION OF EXPERIMENTS

This section provides brief summaries of the test hardware, instrumentation, and data acquisition of the flight and wind tunnel tests. Similarities and differences between the two tests will be emphasized.

Flight Test

The flight test data used in the present study were obtained during the NASA/Army UH-60A Airloads Program conducted from August 1993 to February 1994 (Ref. 8). The four-bladed, articulated main rotor system of a UH-60A Blackhawk aircraft consisted of four subsystems: hub, blade pitch controls, bifilar vibration absorber, and main rotor blades. A bifilar pendulum-type vibration absorber system was mounted on top of the hub to reduce 3/rev rotating in-plane loads. Main rotor dampers were installed between each of the main rotor spindles and the hub to restrain lead-lag motion of the main rotor blades during rotation.

Two of the blades were heavily instrumented: one with subminiature pipette-type pressure transducers and one with a mix of strain-gauges and accelerometers. Absolute pressures were measured at nine radial locations. Blade flap bending, chord bending, and torsion moments were measured with two- or four-leg strain-gauge bridges bonded to the second instrumented blade. The gauges were located at the blade root (11.3% radius) and then evenly distributed along the blade at 10% increments of the rotor radius (20% – 90%). Flap bending moments were measured at all nine radial locations. Chord bending moments were measured at eight radial locations with no measurement at 90%R and torsion moments were measured only at 30%R, 50%R, 70%R, and 90%R. Additional instrumentation included strain gauges on the pitch links, lag dampers, and rotor shaft.

All pressure signals were filtered using 550 Hz low-pass 6- pole Butterworth filters and digitized at a rate of 2142 samples/sec/channel. The non-pressure signals were filtered using 110 Hz low-pass 6-pole Butterworth filters and digitized at a rate of 357 samples/sec/channel. For a typical level-flight test condition, a 5 second time slice (approximately 19 revolutions) was stored in the database. For comparison with wind tunnel test data and analyses, the data were corrected for the signal delay caused by the antialiasing filters on top of a zero azimuth reference correction (Ref. 16). A filter correction of 1.7 deg was applied for the pressure channels and a correction of approximately 8.6 deg was applied to all the non-pressure channels from the flight test, including the shaft bending gauge. Additional details on these corrections can be found in Ref. 15.

Wind Tunnel Test

The NFAC test (Ref. 14) used the same four rotor blades flown during the Airloads Program flight test. The remaining rotor

system hardware was predominantly UH-60A flight hardware (although not the same as used in flight), including spindles, hub, pitch links, and swashplate. For this test, the bifilar four-arm plate was installed but the pendulum weights were not attached (no 3/rev in-plane load absorption).

The rotor assembly was mounted on a large test stand with its own fixed system controls and rotor drive system (transmission, electric motors). The interface between the UH-60A rotor and test stand occurred at three locations: the UH-60A shaft extender and test stand shaft, the swashplate guide and transmission, and the non-rotating swashplate and the fixed system controls. The rotor and test stand were installed on a three-strut support system in the NFAC 40- by 80-Foot Wind Tunnel section as shown in Fig. 2.

The rotor blade instrumentation was essentially identical to the flight test, with five additional blade torsion gages installed on the strain-gage blade. Equivalent pitch link, damper, and shaft bending gages were also installed. The test stand included a rotor balance and flex-coupling to provide direct measurements of rotor hub forces/moments and shaft torque. Angle of attack was measured based on model rotation and airspeed based on calibration of wind tunnel wall pressures.

All pressure signals were filtered using 2000 Hz low-pass filters and digitized at a rate of 2048 samples/rev/channel. The non-pressure signals were filtered using 400 Hz filters and digitized at a rate of 256 samples/rev/channel. Corrections for the time delay caused by the anti-aliasing filters were incorporated in the data reduction process. A typical NFAC test point consisted of 128 revolutions of data.

The major differences between the flight and wind tunnel test mechanical system configurations can be categorized as differences in the drive train dynamics, impedance of the hub and control system, and effects of the bifilar absorber on the hub. In terms of aerodynamic condition, the differences are the aerodynamic inflow field caused by fuselage and LRTA faired body and wall effects of the wind tunnel.

Matched Conditions

During the wind tunnel test, data were acquired at three conditions matching those tested during the Airloads Program. This section describes the specific trim and flight parameters that were matched during the wind tunnel test and similarities and differences in the measured loads between the two tests.

During the wind tunnel test, specific non-dimensional flight parameters and trim targets were matched. The trim targets were rotor thrust (C_T/σ) and hub rolling and pitching moments (C_{Mx}/σ and C_{My}/σ) derived from the rotating shaft bending gage. The flight operating conditions were tip Mach number (M_{tip}), advance ratio (μ), and wind tunnel corrected rotor shaft angle (α_c). There are uncertainties in the parameters for this matching process. Of these parameters, the one with the highest uncertainty from the flight test was rotor thrust. The parameter with the highest uncertainty when set in the wind tunnel was the corrected rotor shaft angle. Because there was no direct measure of rotor thrust in flight, it

was estimated from known quantities. The main rotor lift (i.e. cosine component of the main rotor thrust) is estimated by subtracting fuselage lift, stabilator lift, and canted tail rotor lift from gross weight (Refs. 13, 17). When testing in a wind tunnel, the wind tunnel walls alter the streamlines around the model and change the loads and effective angle of attack on the model. A wind tunnel wall correction, in the form of an induced angle correction, was used to estimate the change in angle of attack of the model due to the tunnel walls (Ref. 18). To account for these and other uncertainties in the trim and operating conditions, the wind tunnel test obtained the baseline data by matching the estimated flight conditions and then acquired additional data for derivative points around this baseline. These derivatives included changes in thrust, hub moments (pitching and rolling), and shaft angle.

Three flight test points were simulated during the wind tunnel testing and the trim and operating conditions for these matched data sets are provided in Table 1. During post-test analysis of the data, it was found that some of the original flight trim targets had been incorrectly specified. That is why the rotor hub moments do not exactly match the trim targets. Nevertheless, the trim values remained relatively close and are well within the trim range from the derivative points. The effects of these trim differences are small for the airloads and structural loads data which are used in this paper.

As an example, comparisons of oscillatory structural load time histories (with means removed) between the flight test (C8424) and wind tunnel test (R47P21) condition are provided in Fig. 3. The C8424 stands for flight counter 84, data point 24 and the R47P21 for wind tunnel run 47, data point 21. The normalized flap bending moment at 60%R and torsion moment at 30%R match very well between the two tests. However, the chord bending moment at 60%R does not match nearly as well as the flap and torsion moments. In particular, the wind tunnel data show lower amplitudes as well as some phase differences.

Figure 4 provides the half peak-to-peak and harmonic magnitude of chord bending moments along the blade span. The differences between the flight and wind tunnel tests are clearly demonstrated in this figure. The flight test had higher 1/rev and 2/rev magnitudes for all radial stations. The 3/rev magnitudes matched well but the 4/rev and 5/rev were significantly different. In particular, the flight test had higher 4/rev magnitudes over the entire blade, while the wind tunnel had higher 5/rev magnitudes outboard of $r/R=0.20$. Reference 15 explained that the differences in 1/rev and 2/rev chord bending are most likely due to differences in installed lag damper characteristics/response. It was also recommended that the potential effects of the drive train dynamics and in-plane hub motion be further investigated in order to understand why the significant differences occurred at 4/rev and 5/rev.

This paper focuses on the advance ratio of 0.3 cases (C8424 and R47P21) and presents the detailed analyses and comparisons with the test data.

DESCRIPTION OF ANALYTICAL METHODS

The analytical results were obtained using the comprehensive analysis RCAS and coupled Helios/RCAS. Descriptions of each analysis and how they are coupled to produce a higher fidelity solution are provided in this section.

RCAS

Rotorcraft Comprehensive Analysis System (RCAS) (Ref. 19) is a comprehensive multidisciplinary, computer software system for predicting rotorcraft aerodynamics, performance, stability and control, aeroelastic stability, loads, and vibration. RCAS is capable of modeling a wide range of complex rotorcraft configurations operating in hover, forward flight, and maneuvering conditions. The RCAS structural model employs a hierarchical, finite element, multibody dynamics formulation for coupled rotor-body systems. It includes a library of primitive elements including nonlinear beams, rigid body mass, rigid bar, spring, damper, hinges and slides to build arbitrarily complex models. RCAS has been used recently for performance, airloads, and structural loads analyses of various rotors including the UH-60A (Refs. 13, 20, 21).

The structural model of the UH-60A rotor employed in this study was validated based on the prescribed measured airloads. Ho et al. (Ref. 22) specified measured airloads from flight test (Ref. 8) as prescribed external loads and then compared the resulting structural response with the measured response. The close agreement between the RCAS calculations and test data provides significant confidence in the structural dynamics modeling and analysis methodology. The same RCAS alone analysis with the prescribed measured airloads is also conducted in this paper for the flight and wind tunnel matched conditions.

For the present analysis, the blade is composed of 13 nonlinear beam elements and 26 aerodynamic panels, called aerosegments. A series of rigid bars and spring elements are used to represent the pitch control linkage. Detailed rotor pitch control system linkage geometry, stiffness, and nonlinear lag damper (based on nonlinear force-velocity relationships) are also incorporated. However, the analytical model does not include stand dynamics nor drive train dynamics. The swashplate flexibility is not modeled. Thus, the pitch link flexibility represents all flexibility of the control system. No bifilar model was incorporated in the analyses for either flight or wind tunnel tests.

Helios

The coupled CFD/CA analyses presented herein were performed using the DoD Computational Research and Engineering Acquisition Tools and Environments Air Vehicles (CREATETM-AV) Helios version 6 software. Helios (HELicopter Overset Simulations) is the rotary-wing product of the US Army and CREATE-AV program sponsored by

the DoD High Performance Computing Modernization Office (Refs. 23–25). Helios uses an innovative multi-mesh paradigm that uses unstructured and/or structured meshes in the near-body close to the solid surfaces to capture the wall-bounded viscous effects and Cartesian grids in the off-body to resolve the wake through a combination of higher-order algorithms and adaptive mesh refinement (AMR). An overset procedure facilitates data exchange and also enables relative motion between meshes. The parallel domain connectivity solver PUNDIT (Parallel UNsteady Domain Information Transfer) automatically handles data exchange between oversetting meshes. CFD is loosely coupled with comprehensive analysis RCAS to solve the rotorcraft structural dynamics and trim. A lightweight Python-based software integration framework orchestrates data exchange between the modules.

The OVERFLOW (Ref. 26) near-body solver is used for the blade meshes in this study. A fifth-order central difference scheme is used for spatial discretization. Second and 6th-order artificial dissipation terms are added to make the scheme stable. For temporal discretization, a second-order accurate diagonalized Beam Warming pentadiagonal scheme is used along with a dual-time algorithm and sub-iterations. For turbulence modeling, the one-equation Spalart-Allmaras model is used.

The Cartesian off-body solver in Helios, SAMCart, is a combination of the block structured meshing infrastructure SAMRAI and a new Cartesian off-body solver (Ref. 25). The off-body CFD solver used here is a temporally third-order explicit Runge-Kutta time integration scheme and a fifth-order central difference spatial scheme with scalar artificial dissipation similar to the OVERFLOW solver. The inviscid Euler equations are solved in the off-body.

The computational grids model the UH-60A blade geometry, but do not include a hub, the LRTA, or the wind tunnel walls in the wind tunnel configuration, or the UH-60A hub and fuselage in flight. The main near-body blade grid for each rotor blade has 265 points chordwise, 189 points along the span, and 69 points in the normal direction using an O-mesh topology. The blade grid is overset with a root cap and a tip cap grid. There are 4.6 million points per blade. The off-body grid has 7 levels of fixed refinement resulting in a finest level grid spacing of approximately 7% chord (1.5 inches) and a total of 74 million nodes. All simulations were carried out for 3.5 rotor revolutions using a time step of 0.25° in CFD. Within each time step, 30 dual-time sub-iterations were used in the near-body grids and 5 explicit sub-steps in the off-body grids. Solutions were run on 192 processors.

Coupling procedure and trim

The CFD/CA coupling procedure in this paper uses the standard loose or delta coupling approach (Ref. 1). Comprehensive analysis RCAS solves for the rotor structural dynamics and trim. High-fidelity CFD analysis was performed using Helios/OVERFLOW. At each coupling iteration the aerodynamic loads calculated by OVERFLOW are passed to RCAS.

After trimming with the OVERFLOW airloads increment, RCAS computes the blade deflections relative to the blade frame of reference and passes them back to OVERFLOW. The coupling between CFD and CA was done at every 90° rotor azimuth. The airloads and blade motions at consecutive coupling CFD/CA iterations converged after 3.5 rotor revolutions. While an azimuthal step size of 0.25° (1440 steps per rotor revolution) was used in the Helios calculations, a 5.0° (72 steps per rotor revolution) azimuthal step size was used for the structural dynamic calculations in RCAS. The trim parameters used in the predictions were the same as those from the test, including non-dimensional rotor thrust, and hub rolling and pitching moments. In addition, rotor blade tip Mach number, advance ratio, and shaft angle of attack were specified.

Prescribed measured airloads

Structural loads are also calculated by applying measured airloads from the tests as prescribed external loads. By prescribing the measured airloads, the coupled aeroelastic response problem is reduced to one involving only structural dynamics. This may help to identify whether sources of inaccuracies in the structural loads prediction originate from deficiencies in aerodynamics or structural dynamics.

For the present analysis, measured blade section normal force, chord force, and pitching moment are prescribed along the blade span to an isolated single-bladed rotor. Measured airload data are available at nine radial locations, and so interpolated airloads, by cell averaging, are prescribed at 26 radial locations. The blade pitch controls are also prescribed. The motion of the pitch control slide element in RCAS, which is located at the base of the pushrod, is adjusted to match with the measured collective and 1/rev cyclic angles at the pitch bearing. The azimuthal resolution of the analysis is 1.5 deg, which is same as the airloads resolution for the flight test.

RESULTS AND DISCUSSION

In this section, selected data from the flight (C8424) and wind tunnel test (R47P21) are compared with predictions from both coupled Helios/RCAS analysis and RCAS analysis with prescribed measured airloads. For both analyses, the effects of the lag damper model are examined by calculating lag damper loads using a nonlinear lag damper model or by applying measured lag damper loads as prescribed external loads.

Flight test condition, C8424

Coupled Helios/RCAS analysis Figure 5 shows nondimensional blade section normal force and pitching moment at 77.5% and 96.5% radial locations. The black solid lines indicate the measured data from the flight test, the dotted blue lines represent the Helios/RCAS analysis results with the nonlinear lag damper model (damper loads calculated), and the red solid lines represent the Helios/RCAS analysis results with the prescribed measured lag damper loads (damper loads

prescribed). Mean values were removed for the pitching moments because errors in the trailing-edge pressure taps can have large effects on integrated section pitching moments. At high speed, the airloads on the blade tip region are generally characterized by negative lift at the end of the first quadrant and the beginning of the second quadrant. The coupled analysis accurately captures this trend, with a steady offset. Some of the small, high-frequency oscillations in the test data in the first quadrant resulting from the wake interaction are also captured in the coupled solution. It is well known that the phase of the airloads from the coupled analysis is significantly improved over comprehensive analysis with lifting-line aerodynamics. However, the phase correlation is not perfect. The coupled analysis tends to overpredict the magnitudes of advancing blade pitching moments and peak-to-peak magnitude at 77.5%R, but underpredict them at 96.5%R.

Figure 6(a) compares the Helios/RCAS calculated oscillatory damper loads with the measured data. The calculated damper loads underpredict the peak-to-peak amplitude and show a phase difference. However, these differences made a negligible impact on the airloads calculations shown in Fig. 5. Figure 6(b) will be explained later.

Figure 7 compares the calculated and measured oscillatory structural loads. Mean values were removed from both test data and analyses. Again, the dotted blue lines represent the Helios/RCAS analysis results with the nonlinear lag damper model (damper loads calculated) and the red solid lines represent the Helios/RCAS analysis results with the prescribed measured lag damper loads (damper loads prescribed). Figures 7(a), 7(d), and 7(g) show the oscillatory flap bending moments at 11.3%R, 30%R, and 60%R, respectively. The coupled analysis shows reasonably good correlation with the flight test data. The peak-to-peak amplitude is well predicted but there is an approximate 10-deg phase difference between the data and analysis. Lag damper loads (calculated vs. prescribed) are important only for the most inboard radial location.

Figures 7(b), 7(e), and 7(h) show the oscillatory torsion moments at 30%R and 70%R and pitch link load, respectively. The behaviors of torsion moments at 30%R and pitch link loads, which are interdependent, are predicted reasonably well in the first and second quadrants, but are not satisfactory in the third and fourth quadrants. In general, the torsion moment correlation at 70%R is worse than that at 30%R. The effects of the lag damper loads on the torsion moments are very small.

Figures 7(c), 7(f), and 7(i) show the oscillatory chord bending moments at 11.3%R, 30%R, and 60%R, respectively. As expected, the lag damper loads have more influence on the chord bending moments than the flap bending and torsion moments. The correlation of the chord bending moment at 11.3%R is excellent with the prescribed measured damper loads. The analysis with the nonlinear lag damper model shows worse correlation at 11.3%R in both waveform and phase due to the inaccurate lag damper loads prediction shown in Fig. 6(a). Better waveform and peak-to-peak correlation

were observed at 30%R with the prescribed measured damper loads. Both lag damper models, however, significantly underpredict the magnitude of chord bending moment at 60%R.

Chord bending moment, which is a main focus of this study, is further examined. Figure 8 compares the half peak-to-peak and harmonic magnitude of chord bending moments along the blade span. Chord bending moments are strongly affected by the damper loads. The analysis with the prescribed measured lag damper loads increases the half peak-to-peak magnitudes and thus improves the correlation compared to that with the nonlinear damper model. Even with the improvement, there is still a significant underprediction. Previous analysis of the UH-60A rotor using Helios/RCAS examined the difference between linear and nonlinear lag damper models (Ref. 13). The study showed that 1) lag damper modeling has an important influence near the root of the blade and its effect diminishes around mid span and 2) lag damper modeling did not affect the 4/rev chord bending moments and both the linear and nonlinear lag damper models significantly underpredict the 4/rev harmonic magnitude. Unlike those observations, the present analysis with the prescribed measured damper loads increases the 4/rev harmonic component around the mid span and thus meaningful improvement is obtained.

RCAS analysis with prescribed measured airloads This subsection investigates the structural loads calculated from the prescribed measured airloads (normal force, chord force, and pitching moment) using RCAS alone. Structural loads are calculated for C8424 and the results are compared with the measurements in Fig. 9. Again, the effects of lag damper are examined by using either the nonlinear lag damper model (damper loads calculated) or prescribing the measured lag damper loads (damper loads prescribed) in addition to the measured airloads. Figure 6(b) compares the RCAS calculated damper loads with the measured damper loads.

Calculated and measured flap bending moments shown in Figs. 9(a), 9(d), and 9(g) are in good agreement, and the excellent magnitude and phase correlation at 30%R is noteworthy. The flap bending moment correlation at 60%R is also significantly improved in both magnitude and phase compared to the Helios/RCAS analysis shown in Fig. 7(g). This shows the importance of airloads for accurate prediction of flap bending moments. Figures 9(b), 9(e), and 9(h) show the oscillatory torsion moments at 30%R and 70%R and pitch link load, respectively. The analysis with the prescribed measured airloads shows slightly better correlation than the coupled analysis on the retreating side. However, the overall correlation did not improve much. In general, the effects of the lag damper on the torsion moments are very small. Figures 9(c), 9(f), and 9(i) show the oscillatory chord bending moments at 11.3%R, 30%R, and 60%R, respectively. The calculations and measurements agree very well for the chord bending moments at 11.3%R, but the correlation gets worse for the outboard locations. Again, the analysis with the measured airloads improves the chord bending moment correlation compared to the coupled Helios/RCAS analysis.

Figure 10 compares the half peak-to-peak and harmonic magnitude of chord bending moments along the blade span. For the calculated lag damper load case, the results with the prescribed measured airloads show much better correlation with the measured data compared to those with the Helios/RCAS analysis shown in Fig. 8, mostly because 1, 3, and 4/rev harmonic magnitudes increased. Although the 4/rev harmonic magnitude is still substantially underpredicted even with the increased magnitude observed, the results show the importance of airloads for the prediction of the 4/rev harmonic and thus overall chord bending moments. For the prescribed measured lag damper loads case, the half peak-to-peak value did not change much compared to the Helios/RCAS analysis. However, the correlation of 3 and 4/rev harmonic magnitudes is significantly improved. These results indicate the importance of lag damper loads on the chord bending moment correlation. A drive train model may be needed to better match with the 4/rev harmonic magnitude but its effects might be smaller than what was suggested in Ref. 13.

Wind tunnel test condition, R47P21

This section examines the wind tunnel test data and focuses on the chord bending moments, as both flap bending and torsion moment results are very similar to those in the flight test section.

Coupled Helios/RCAS analysis Figure 11 shows nondimensional blade section normal force and pitching moment at 77.5% and 96.5% radial locations. The predicted section normal force and pitching moment for the wind tunnel test are almost identical to those for the flight test because the trim and operating conditions are matched. The measured data between the tests agree very well at 77.5%R, but show some differences at 96.5%R. The overall correlation at 77.5%R is same as for the flight test. However, the coupled analysis better predicts the magnitude and phase of the negative lift for the wind tunnel test than for the flight test shown in Fig. 5. Pitching moment correlation at 96.5%R is also improved compared to the flight test.

Figure 12(a) compares the Helios/RCAS calculated oscillatory damper loads with the measured data. The calculated damper loads shows reasonably good correlation of the peak-to-peak amplitude but were not able to accurately capture the waveform. Figure 12(b) will be explained later.

Figure 13 compares the calculated and measured oscillatory chord bending moments at 11.3%R, 30%R, and 60%R, respectively, with damper loads calculated with the nonlinear lag damper model and damper loads prescribed with the measured values. The Helios/RCAS analysis with the nonlinear lag damper shows reasonably good correlation of the chord bending moment at 11.3%R on the retreating side, but the waveform on the advancing side is not accurately captured. This is consistent with the lag damper load correlation shown in Fig. 12(a). The correlation of the chord bending moment at 11.3%R is excellent on both advancing and retreating sides

with the prescribed measured damper loads. However, neither model was able to accurately predict the waveforms at 30%R and 60%R. Nonetheless, correlation for the wind tunnel test is better than that for the flight test shown in the right column of Fig. 7. As the predicted chord bending moments did not change much, the reason for the better correlation is because of the changes in the measured data from the flight to the wind tunnel test.

Figure 14 compares the half peak-to-peak and harmonic magnitude of chord bending moments along the blade span. Predicted chord bending moment harmonics correlate reasonably well with the measured harmonics for the most part. This correlation is much better than the correlation with the flight test data shown in Fig. 8. The half peak-to-peak and 1 and 2/rev harmonic magnitudes did not change much between the damper loads calculated with the nonlinear lag damper model and the damper loads prescribed with the measured loads. The 3/rev harmonic magnitude is better predicted with the nonlinear lag damper model and 4 and 5/rev harmonic magnitudes are better predicted with the prescribed measured lag damper loads.

RCAS analysis with prescribed measured airloads Figure 15 compares the calculated and measured oscillatory chord bending moments at 11.3%R, 30%R, and 60%R, respectively, with the prescribed measured airloads. For the nonlinear lag damper case (the calculated damper loads are shown in Fig. 12(b)), the results show much better correlation with the measured data compared to those with the Helios/RCAS analysis (Fig. 13). The correlation of the chord bending moment at 11.3%R is excellent with the prescribed measured damper loads. The correlation on the retreating side is also excellent at 30%R and 60%R with the prescribed measured damper loads.

Figure 16 compares the half peak-to-peak and harmonic magnitude of chord bending moments along the blade span. The predicted half peak-to-peak and harmonics magnitudes correlate well with the measured values for the most part with the prescribed lag damper loads. In particular, the 4 and 5/rev harmonic correlation is excellent.

The calculated chord bending moments with the prescribed measured airloads and measured damper loads show the best correlation with the wind tunnel test data. This again confirms that both airloads and damper loads are important for the accurate prediction of chord bending moments. The wind tunnel correlation results suggest that other possible effects (drive train, hub impedance) may not be significant factors for the wind tunnel configuration (although these could be compensating effects). The differences between the flight and wind tunnel correlation suggest that these other factors may still be important for the flight test vehicle.

CONCLUSIONS

This paper investigates the UH-60A rotor structural loads to better understand the differences in chord bending moments

between the flight and full-scale wind tunnel tests. Coupled Helios/RCAS analysis is performed and the calculated rotor loads are compared with the test data. RCAS alone analysis is also performed by applying measured airloads from the tests as prescribed external loads to help identify whether sources of inaccuracies in the structural loads prediction originate from deficiencies in aerodynamics or structural dynamics. The effects of the lag damper model are examined by calculating lag damper loads using a nonlinear lag damper model or by applying measured lag damper loads as prescribed external loads. From this study the following conclusions are obtained:

1) Although the coupled Helios/RCAS analysis shows reasonably good flap bending moment correlation for the flight test, the flap bending moments calculated from the measured airloads show much better correlation with the test data.

2) The analysis with the measured airloads also improves the chord bending moment correlation compared to the coupled Helios/RCAS analysis. This shows the importance of airloads for the accurate prediction of flap and chord bending moments. The chord bending moment correlation, especially 4/rev harmonic magnitudes, further improves by prescribing the measured lag damper loads.

3) The chord bending moment correlation for the wind tunnel test is much better than that for the flight test. The calculated chord bending moments with the prescribed measured airloads and measured damper loads show the best correlation with the wind tunnel test data. In particular, the 4 and 5/rev harmonic correlation is excellent. These results for the wind tunnel test suggest that the effects of drive train dynamics or hub impedance on the chord bending moments appear to be very small or even negligible for the wind tunnel configuration, although these could be compensating effects.

4) Drive train dynamics or hub impedance are probably important for the flight test data, but their effects on the chord bending moments might be smaller than what was suggested in previous studies.

REFERENCES

- ¹Potsdam, M., Yeo, H., and Johnson, W., "Rotor Airloads Prediction Using Loose Aerodynamic/Structural Coupling," *Journal of Aircraft*, Vol. 43, (3), May-June 2006, pp. 732-742.
- ²Datta, A., Nixon, M., and Chopra, I., "Review of Rotor Loads Prediction with the Emergence of Rotorcraft CFD," *Journal of the American Helicopter Society*, Vol. 52, (4), October 2007, pp. 287-317.
- ³Bhagwat, M. J., Ormiston, R. A., Saberi, H. A., and Xin, H., "Application of Computational Fluid Dynamics/Computational Structural Dynamics Coupling for Analysis of Rotorcraft Airloads and Blade Loads in Maneuvering Flight," *Journal of the American Helicopter Society*, Vol. 57, (3), April 2012.
- ⁴Yeo, H., Potsdam, M., and Ormiston, R. A., "Rotor Aeroelastic Stability Analysis Using Coupled Computational Fluid

Dynamics/Computation Structural Dynamics,” *Journal of the American Helicopter Society*, Vol. 56, (4), October 2011.

⁵Rajmohan, N., Marpu, R. P., Sankar, L. N., Baeder, J. D., and Egolf, T. A., “Improved Prediction of Rotor Maneuvering Loads using a Hybrid Methodology,” American Helicopter Society 67th Annual Forum, Virginia Beach, VA, May 3-5, 2011.

⁶Smith, M. J., Lim, J. W., van der Wall, B. G., Baeder, J. D., Biedron, R. T., Boyd, D. D., Jr., Jayaraman, B., Jung, S. N., and Min, B. Y., “An Assessment of CFD/CSD Prediction State-of-the-Art Using the HART II International Workshop Data,” American Helicopter Society 68th Annual Forum Proceedings, Fort Worth, TX, May 1-3, 2012.

⁷Ortun, B., Potsdam, M., Yeo, H., and Truong, V. K., “Rotor Loads Prediction on the ONERA 7A Rotor using Loose Fluid/Structure Coupling,” American Helicopter Society 72nd Annual Forum Proceedings, West Palm Beach, FL, May 17-19, 2016.

⁸Bousman, W. G., and Kufeld, R. M., “UH-60A Airloads Catalog,” NASA TM-2005-212827, August 2005.

⁹Sitaraman, J., Datta, A., Baeder, J., and Chopra, I., “Coupled CFD/CSD prediction of Rotor Aerodynamic and Structural Dynamic Loads for Three Critical Flight Conditions,” 31st European Rotorcraft Forum, Florence, Italy, September 13-15, 2005.

¹⁰Biedron, R. T., and Lee-Rausch, E. M., “Computation of UH-60A Airloads Using CFD/CSD Coupling On Unstructured Meshes,” American Helicopter Society 67th Annual Forum, Virginia Beach, VA, May 3-5, 2011.

¹¹Datta, A., and Chopra, I., “Prediction of the UH-60A Main Rotor Structural Loads Using Computational Fluid Dynamics/Comprehensive Analysis Coupling,” *Journal of the American Helicopter Society*, Vol. 49, (4), October 2008, pp. 351-365.

¹²Zhao, J., and He, C., “Rotor Blade Structural Loads Analysis Using Coupled CSD/CFD/VVPM,” American Helicopter Society 69th Annual Forum, Phoenix, AZ, May 21-23, 2013.

¹³Yeo, H., and Potsdam, M., “Rotor Structural Loads Analysis Using Coupled Computational Fluid Dynamics/Computational Structural Dynamics,” American Helicopter Society 70th Annual Forum, Montréal, Québec, Canada, May 20-22, 2014.

¹⁴Norman, T. R., Shinoda, P. M., Peterson, R. L., and Datta, A., “Full-scale Wind Tunnel Test of the UH-60A Airloads Rotor,” American Helicopter Society 67th Annual Forum, Virginia Beach, VA, May 3-5, 2011.

¹⁵Norman, T. R., Peterson, R. L., Maier, T. H., and Yeo, H., “Evaluation of Wind Tunnel and Scaling Effects with the UH-60A Airloads Rotor,” American Helicopter Society 68th Annual Forum Proceedings, Fort Worth, TX, May 1-3, 2012.

¹⁶Kufeld, R. M., and Bousman, W. G., “UH-60A Airloads Program Azimuth Reference Correction,” *Journal of the American Helicopter Society*, Vol. 50, No. 2, April 2005, pp. 211-213.

¹⁷Tung, C., Bousman, W. G., and Low, S., “A Comparison of Airload Data Between Model-Scale Rotor and Full-Scale Flight Test,” American Helicopter Society Aeromechanics and Product Design, Bridgeport, CT, October 11-13, 1995.

¹⁸Langer, H. J., Peterson, R. L., and Maier, T. H., “An Experimental Evaluation of Wind Tunnel Wall Correction Methods for Helicopter Performance,” American Helicopter Society 52nd Annual Forum, Washington, D.C., June 4-6, 1996.

¹⁹Saberi, H. A., Hasbun, M., Hong, J., Yeo, H., and Ormiston, R. A., “RCAS Overview of Capabilities, Validations, and Applications to Rotorcraft Problems,” American Helicopter Society 71st Annual Forum Proceedings, Virginia Beach, VA, May 5-7, 2015.

²⁰Jain, R., Yeo, H., Bhagwat, M., and Ho, J. C., “An Assessment of RCAS Performance Prediction for Conventional and Advanced Rotor Configurations,” American Helicopter Society 70th Annual Forum Proceedings, Montréal, Québec, Canada, May 20-22, 2014.

²¹Ho, J. C., and Yeo, H., “Assessment of Comprehensive Analysis Predictions of Helicopter Rotor Blade Loads in Forward Flight,” American Helicopter Society 72nd Annual Forum Proceedings, West Palm Beach, FL, May 17-19, 2016.

²²Ho, J. C., Yeo, H., and Ormiston, R. A., “Investigation of Rotor Blade Structural Dynamics and Modeling Based on Measured Airloads,” *Journal of Aircraft*, Vol. 45, (5), September-October 2008, pp. 1631-1642.

²³Wissink, A., Jayaraman, B., Datta, A., Sitaraman, J., Potsdam, M., Kamkar, S., Mavriplis, D., Yang, Z., Jain, R., Lim, J., and Strawn, R., “Capability Enhancements in Version 3 of the Helios High-Fidelity Rotorcraft Simulation Code,” AIAA-2012-0713, 50th AIAA Aerospace Sciences Meeting, January 9-12, 2012, Nashville, TN.

²⁴Jain, R., and Potsdam, M., “Strategies for OVERFLOW Modularization and Integration into HELIOS,” 11th Overset Grid Symposium, Dayton, OH, October 15-18, 2012.

²⁵Wissink, A., Sitaraman, J., Jayaraman, B., Roget, B., Lakshminarayan, V., Potsdam, M., Jain, R., Leffell, J., Forsythe, J. R., and Bauer, A., “Recent Advancements in the Helios Rotorcraft Simulation Code,” AIAA-2016-0563, 54th AIAA Aerospace Sciences Meeting, January 4-8, 2016, San Diego, CA.

²⁶Nichols, R. H., and Buning, P. G., “OVERFLOW User’s Manual, Version 2.2,” NASA Langley Research Center, Hampton, VA, August 2010.

Table 1. Flight and wind tunnel matched conditions.

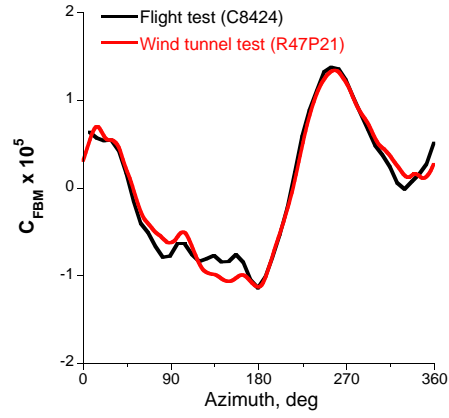
Pt Type	Pt #	M_{tip}	μ	α_c	C_T/σ	C_{Mx}/σ	C_{My}/σ
Flight	C8424	0.637	0.304	-4.32	0.088	-0.00092	-0.00058
Wind tunnel	R47P21	0.637	0.303	-4.16	0.087	-0.00071	-0.00083
Flight	C8525	0.642	0.233	-1.56	0.077	-0.00116	-0.00022
Wind tunnel	R60P18	0.642	0.232	-1.48	0.077	-0.00119	-0.00036
Flight	C9020	0.670	0.244	-0.52	0.118	-0.00059	-0.00012
Wind tunnel	R60P28	0.669	0.245	-0.50	0.118	-0.00059	-0.00016



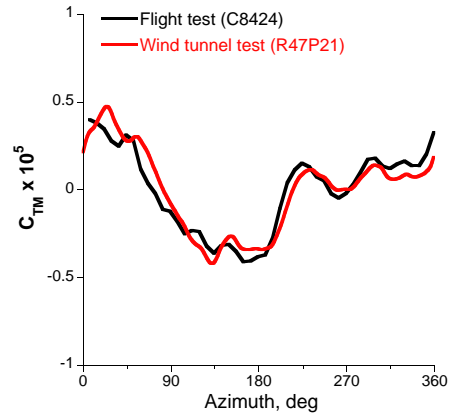
Fig. 1. UH-60A Airloads rotor in flight.



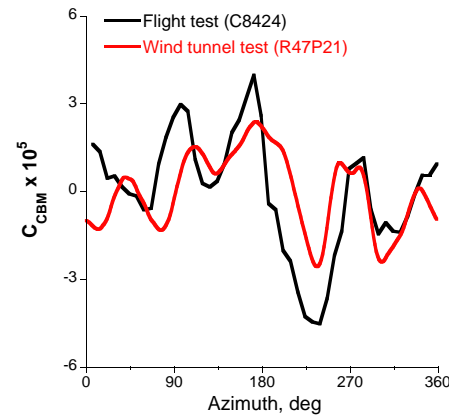
Fig. 2. UH-60A rotor system installed on the Large Rotor Test Apparatus in the NFAC 40- by 80-Foot Wind Tunnel.



(a) Flap bending moment @ 60%R



(b) Torsion moment @ 30%R



(c) Chord bending moment @ 60%R

Fig. 3. Blade structural loads comparison between flight and wind tunnel tests.

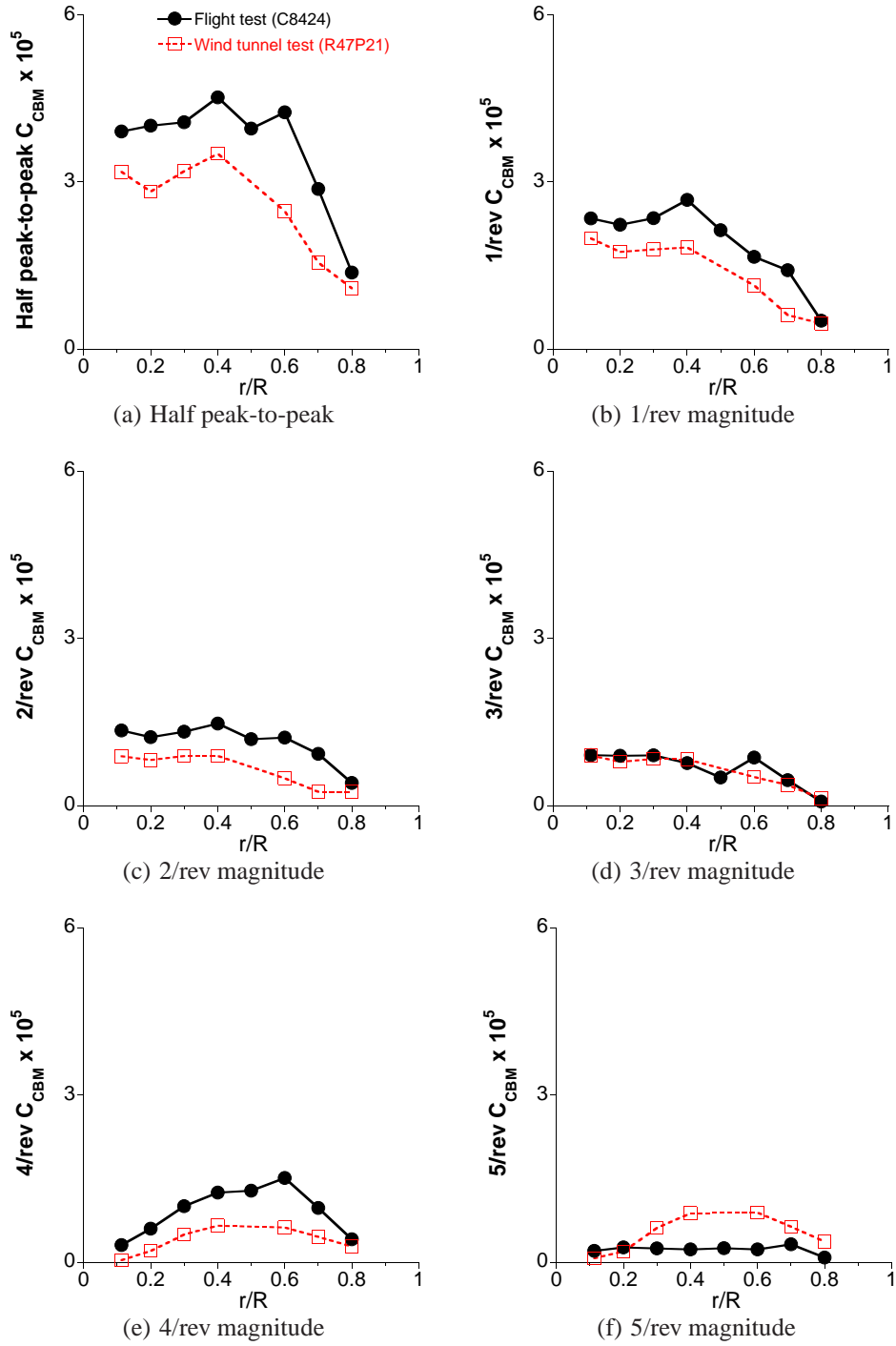


Fig. 4. Half peak-to-peak and harmonic magnitude of chord bending moments comparison between flight and wind tunnel tests.

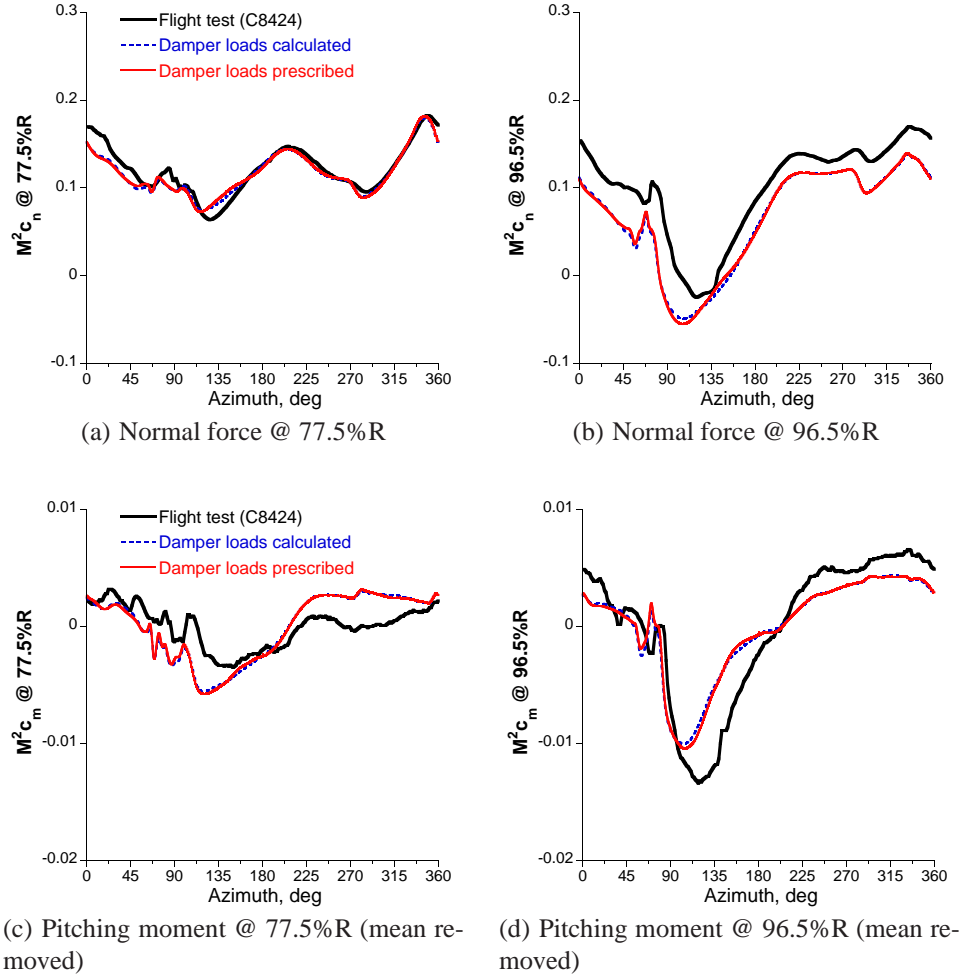


Fig. 5. Blade section normal force and pitching moment from Helios/RCAS, $\mu = 0.304$, $C_T/\sigma = 0.088$ (Flight Test, C8424).

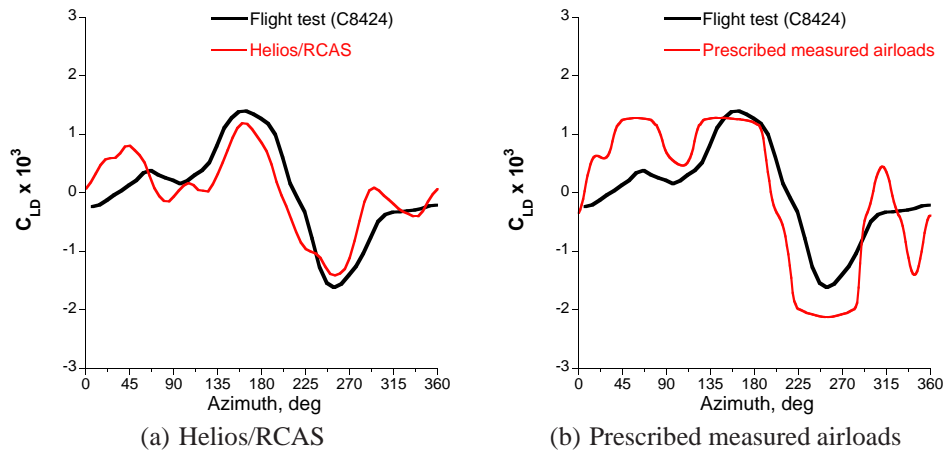
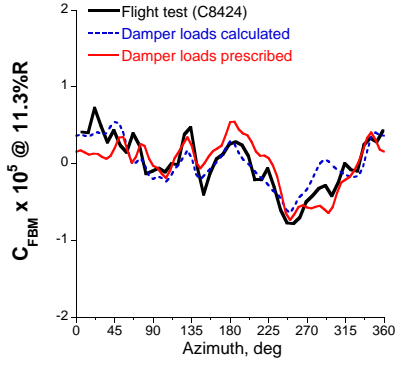
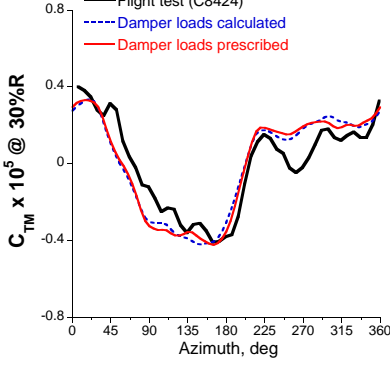


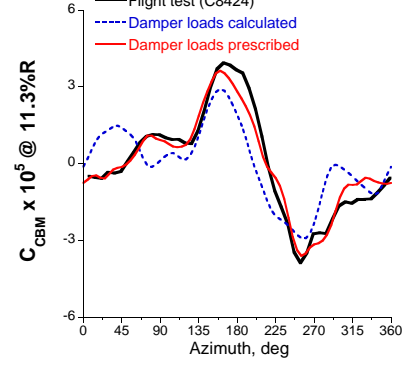
Fig. 6. Comparison of time history of lag damper loads, $\mu = 0.304$, $C_T/\sigma = 0.088$ (Flight Test, C8424) .



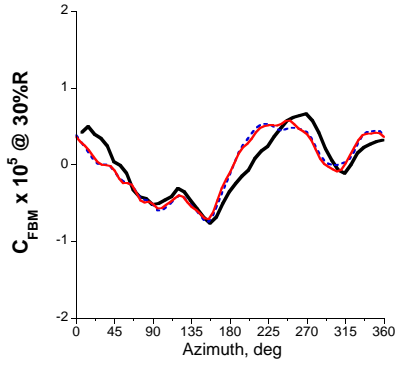
(a) Flap bending moment @ 11.3%R



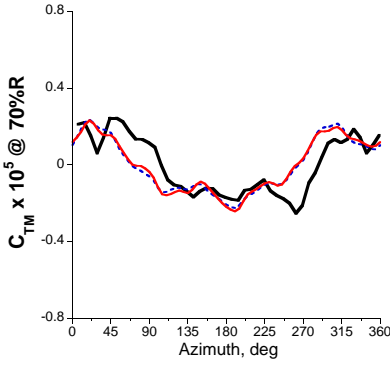
(b) Torsion moment @ 30%R



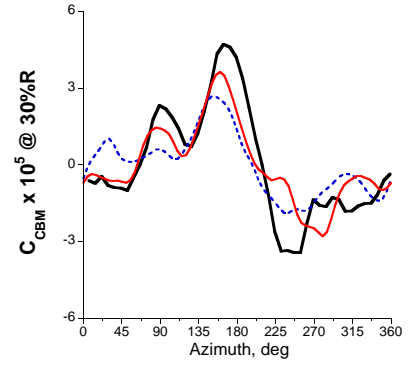
(c) Chord bending moment @ 11.3%R



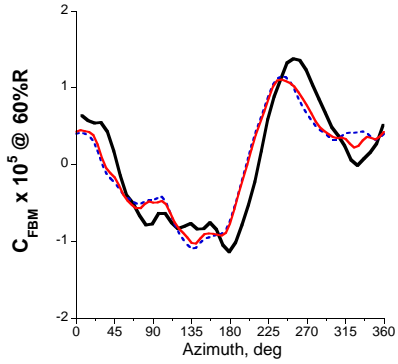
(d) Flap bending moment @ 30%R



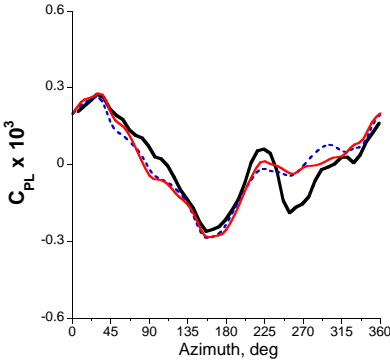
(e) Torsion moment @ 70%R



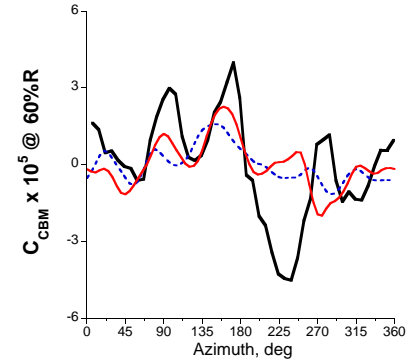
(f) Chord bending moment @ 30%R



(g) Flap bending moment @ 60%R



(h) Pitch link load



(i) Chord bending moment @ 60%R

Fig. 7. Structural loads from Helios/RCAS, $\mu = 0.304$, $C_T/\sigma = 0.088$ (Flight Test, C8424).

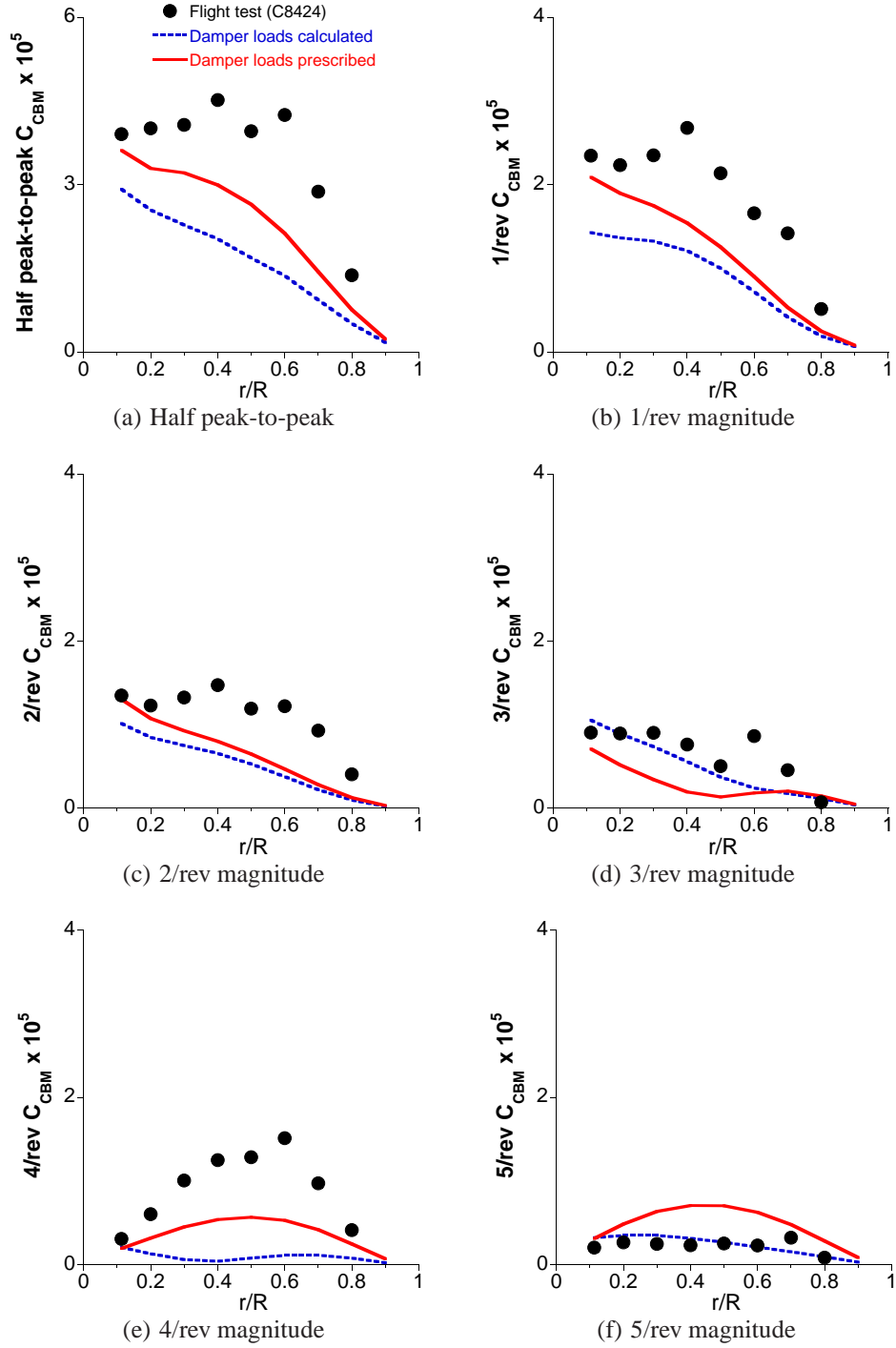
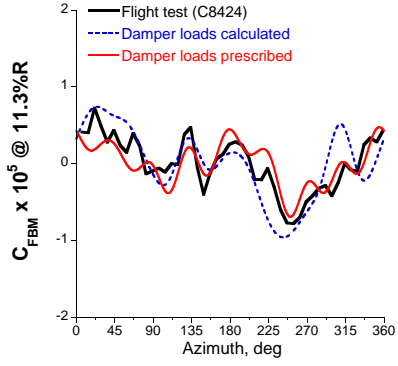
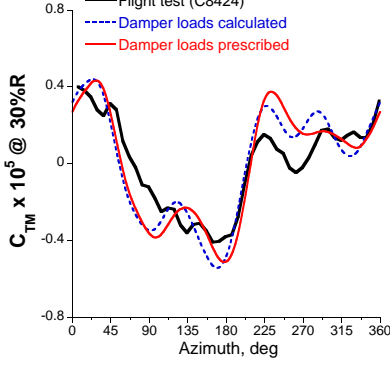


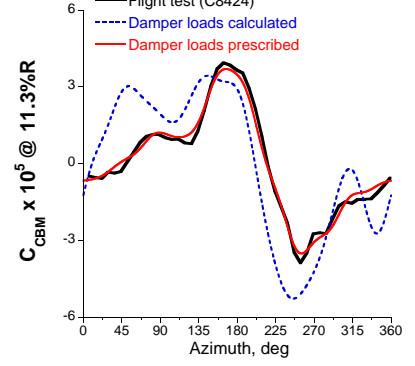
Fig. 8. Half peak-to-peak and harmonic magnitude of chord bending moments from Helios/RCAS, $\mu = 0.304$, $C_T/\sigma = 0.088$ (Flight Test, C8424).



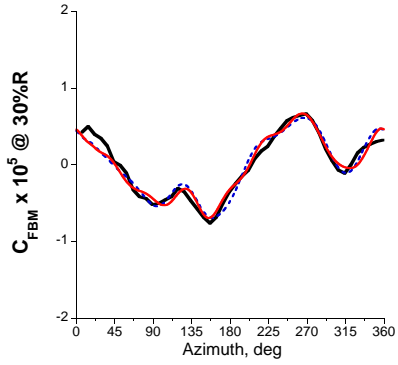
(a) Flap bending moment @ 11.3%R



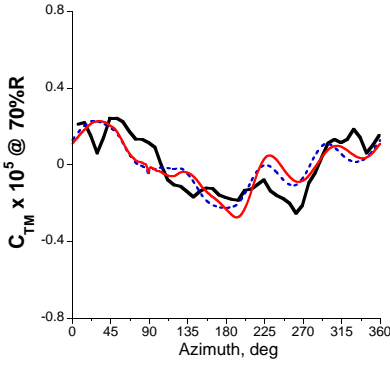
(b) Torsion moment @ 30%R



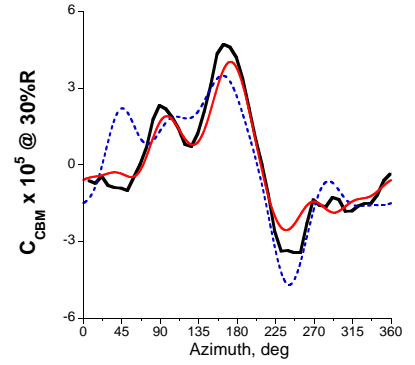
(c) Chord bending moment @ 11.3%R



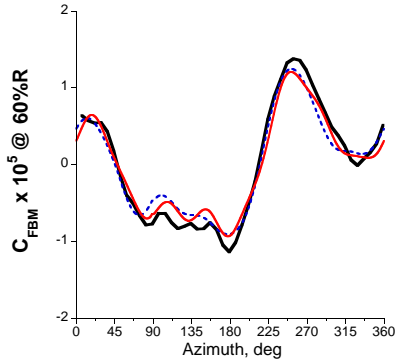
(d) Flap bending moment @ 30%R



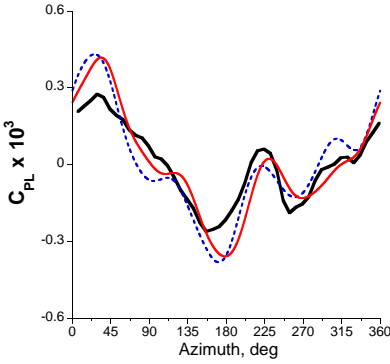
(e) Torsion moment @ 70%R



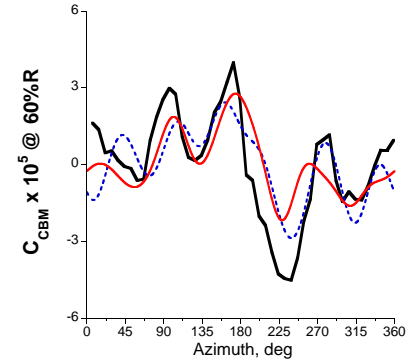
(f) Chord bending moment @ 30%R



(g) Flap bending moment @ 60%R



(h) Pitch link load



(i) Chord bending moment @ 60%R

Fig. 9. Structural loads from prescribed measured airloads, $\mu = 0.304$, $C_T/\sigma = 0.088$ (Flight Test, C8424).

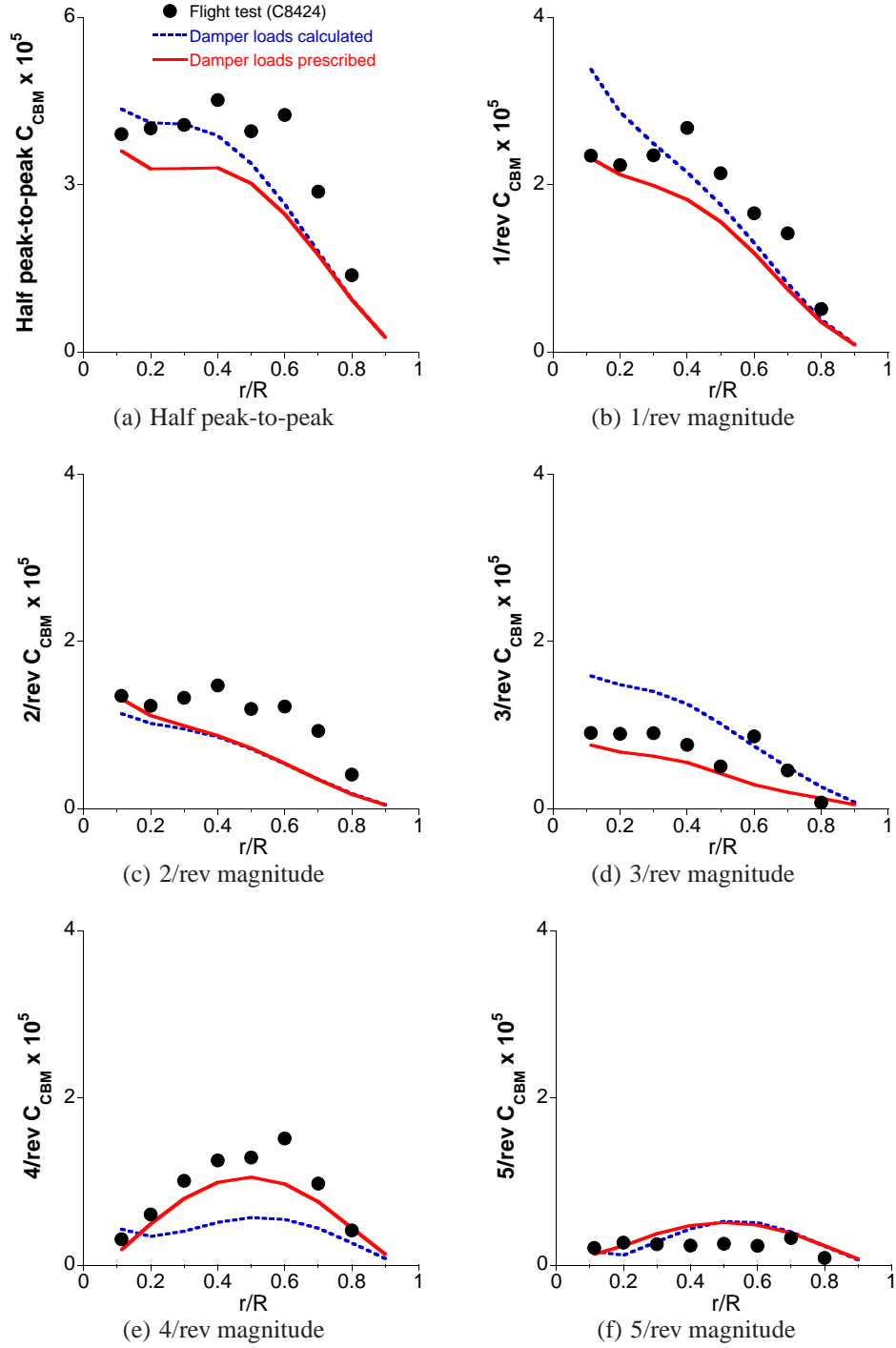


Fig. 10. Half peak-to-peak and harmonic magnitude of chord bending moments from prescribed measured airloads, $\mu = 0.304$, $C_T/\sigma = 0.088$ (Flight Test, C8424).

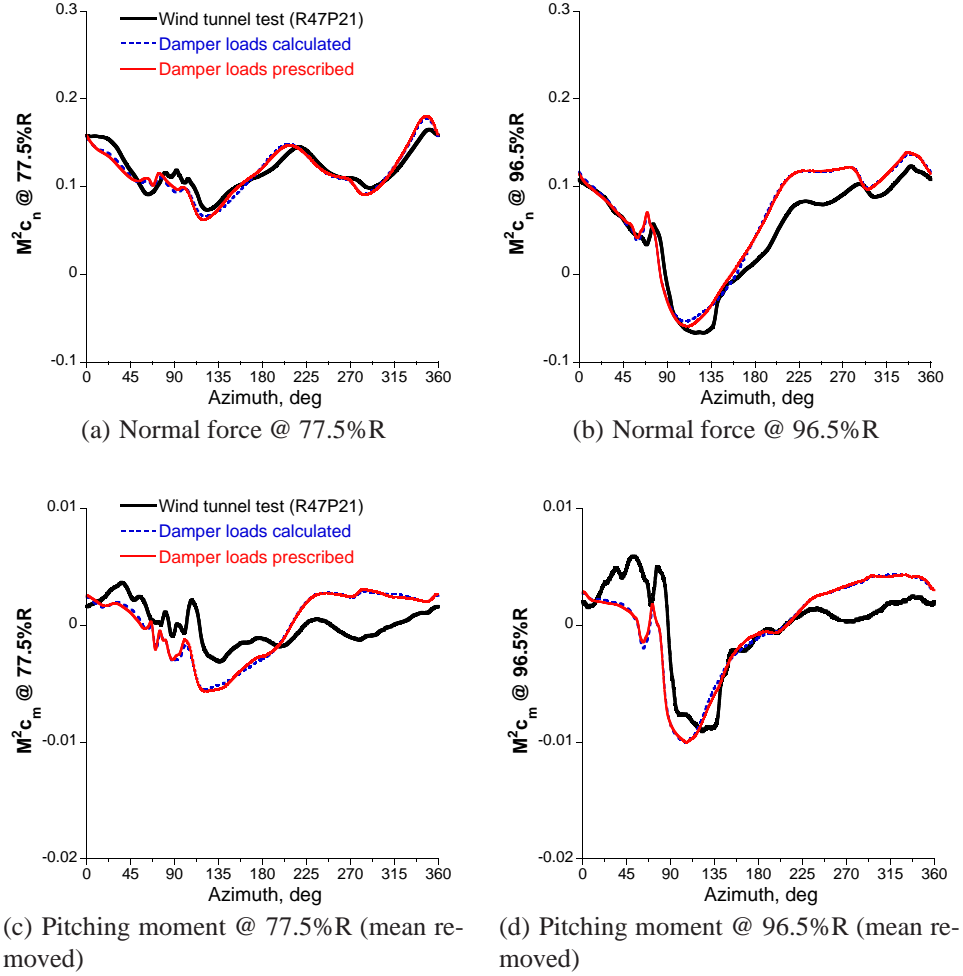


Fig. 11. Blade section normal force and pitching moment from Helios/RCAS, $\mu = 0.303$, $C_T/\sigma = 0.087$ (Wind tunnel test, R47P21).

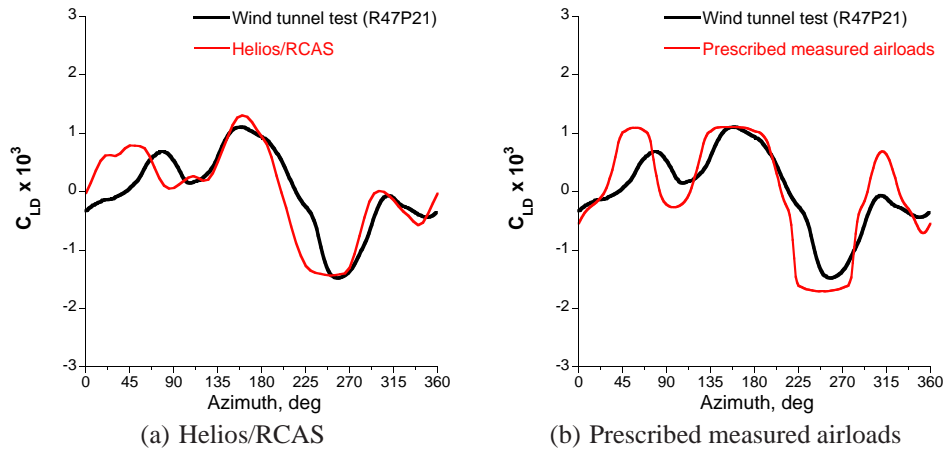
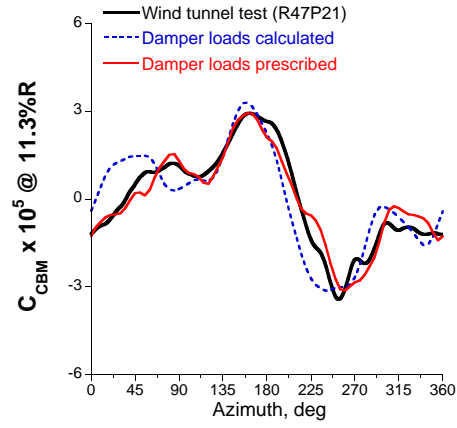
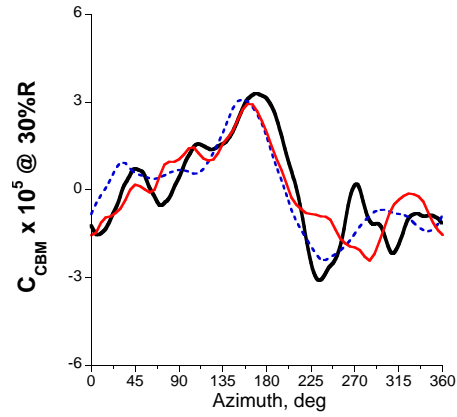


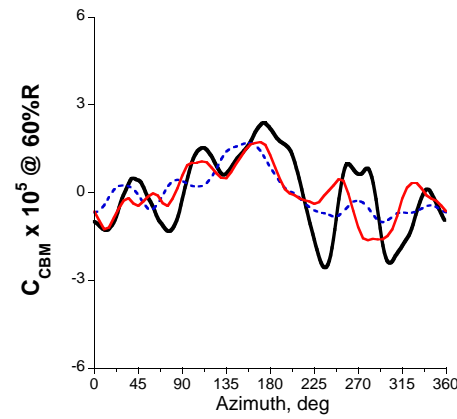
Fig. 12. Comparison of time history of lag damper loads, $\mu = 0.303$, $C_T/\sigma = 0.087$ (Wind tunnel test, R47P21) .



(a) Chord bending moment @ 11.3%R



(b) Chord bending moment @ 30%R



(c) Chord bending moment @ 60%R

Fig. 13. Chord bending moments from Helios/RCAS, $\mu = 0.303$, $C_T/\sigma = 0.087$ (Wind tunnel test, R47P21).

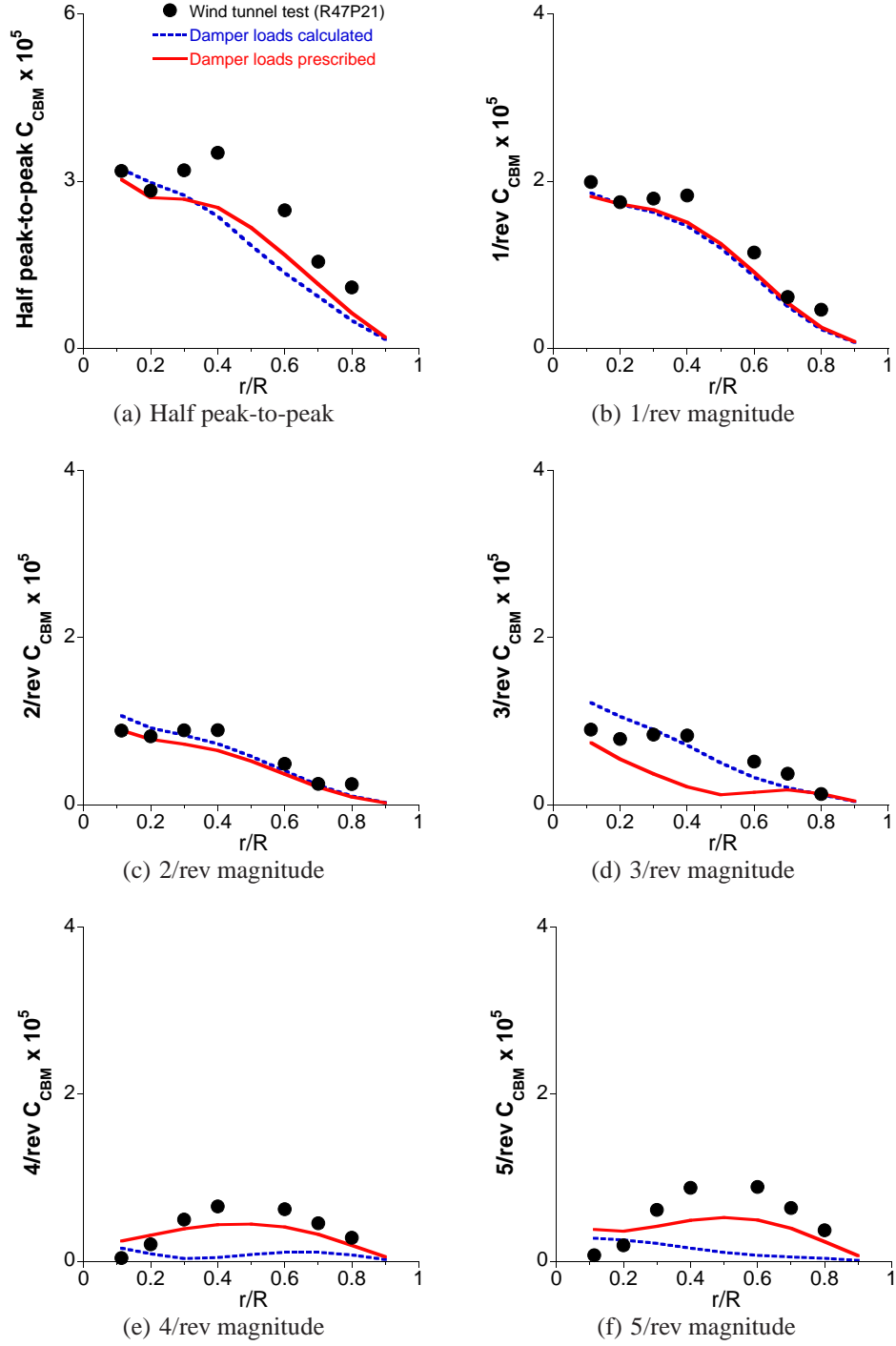
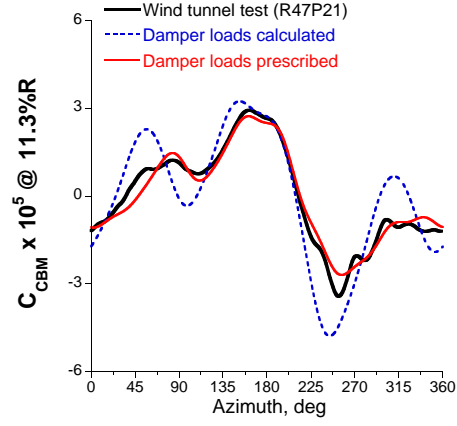
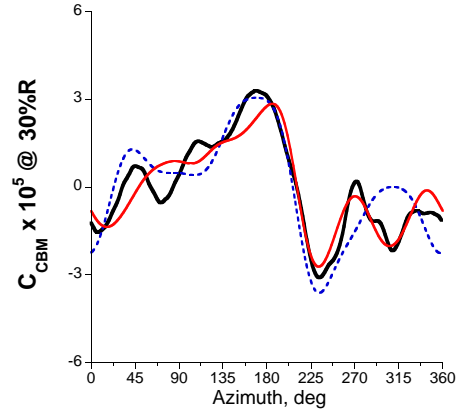


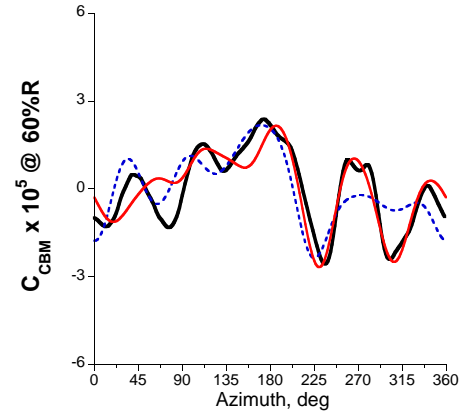
Fig. 14. Half peak-to-peak and harmonic magnitude of chord bending moments from Helios/RCAS, $\mu = 0.303$, $C_T/\sigma = 0.087$ (Wind tunnel test, R47P21).



(a) Chord bending moment @ 11.3%R



(b) Chord bending moment @ 30%R



(c) Chord bending moment @ 60%R

Fig. 15. Chord bending moments from prescribed measured airloads, $\mu = 0.303$, $C_T/\sigma = 0.087$ (Wind tunnel test, R47P21).

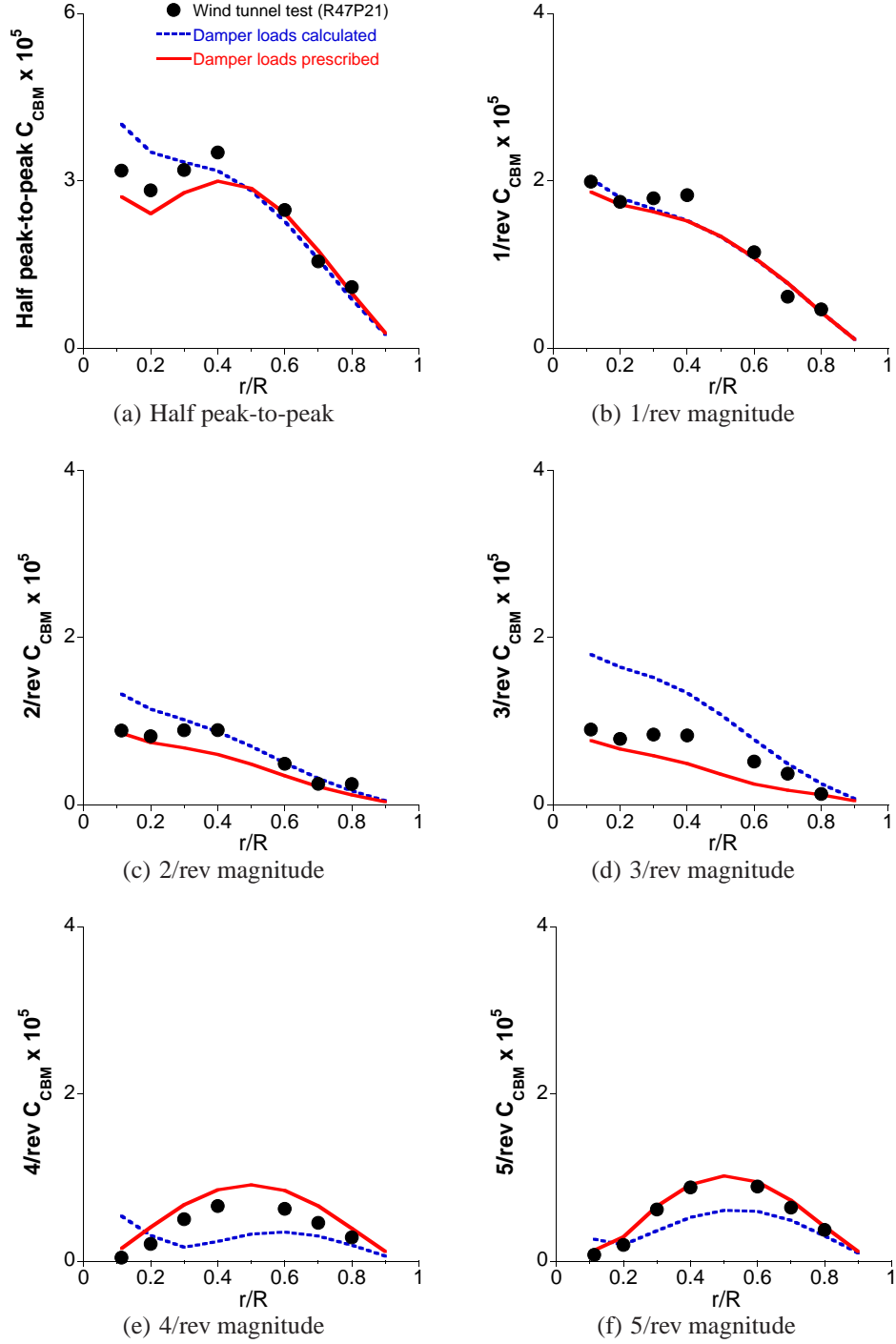


Fig. 16. Half peak-to-peak and harmonic magnitude of chord bending moments from prescribed measured airloads, $\mu = 0.303$, $C_T/\sigma = 0.087$ (Wind tunnel test, R47P21).